RSC Advances

PAPER

View Article Online
View Journal | View Issue

Cite this: *RSC Adv.*, 2021, **11**, 28320

PCN-222@g-C_3N_4 cathodic materials for "signal-off" photoelectrochemical sensing of kanamycin sulfate†

Wenxia Dong,[a] Zhongping Li,*[a] Wen Wen,[a] Sisi Feng,[c] Yuanjian Zhang[d] and Guangming Wen*[ab]

A novel cathodic photoelectrochemical (PEC) sensor was developed for the ultrasensitive detection of kanamycin sulfate (KAM) based on the g-C_3N_4 coupled zirconium-based porphyrinic metal–organic framework (PCN-222). Photocathodes made by double n-type semiconductors, which was attributed to the transfer of electrons and holes from g-C_3N_4 broad band to PCN-222 with narrow band gap. The photocurrent decreased when KAM was added, which was conducive to the construction of the PEC sensor. Then, the PCN-222@g-C_3N_4 was used as a photosensitive platform to construct a label-free strategy and ultrasensitive detection of KAM with wide linear range from 1 to 1000 nM and a low detection limit of 0.127 nM. Moreover, this sensing platform shows good selectivity, favourable reproducibility and brilliant stability. The reported sensors provided great potential for the detection of KAM in actual samples.

Received 2nd June 2021
Accepted 3rd August 2021

DOI: 10.1039/d1ra04275k

rsc.li/rsc-advances

1 Introduction

Kanamycin sulfate (KAM) is a common aminoglycoside antibiotic fabricated by the fermentation of streptomyces kanamyceticus.[1] Due to its strong antibacterial activity and low cost, KAM has been widely used to prevent infections, treat diseases and promote growth.[2,3] The antimicrobial property of KAM is mainly reflected in its ability to induce mistranslation and indirectly inhibit translocation during protein synthesis, resulting in the production of abnormal proteins harmful to bacteria.[4] However, the abuse of antibiotics has caused environmental pollution, leading to the global aggravation in antibiotic resistance. In addition, antibiotics can accumulate through the food chain and eventually transfer to humans, inevitably leading to disease problems such as ototoxicity and nephrotoxicity.[5–8] Therefore, from the perspective of human security and environment safety, it is urgent to establish a sufficiently selective and sensitive method for the detection of KAM residue. Currently, several analytical methods have been developed for the determination of KAM from such as high-performance liquid chromatography method,[9] mass spectrometry method,[10] colorimetric analysis,[11] fluorescence method[12] and electrochemical aptasensors.[13–21] Among them, electrochemical aptamer sensors have attracted more and more attention due to some unique advantages such as high specificity and sensitivity.

Willner *et al.* reported the photoelectric (PEC) chemistry sensor for the first time in 2001, PEC sensing has been extensively studied in different fields.[22–26] Due to the elegant merits of low background, high sensitivity and easy minimization, this technique has unique advantages in the detection of biomolecules and environmental pollutants.[27] The sensing principle mainly depends on the electron transfer among target, semiconductor, and electrode with photoirradiation.[28] The photoelectric material will generate an electric current under illumination, and the final detection signal as the form of electrochemical expression.[29] Generally, PEC sensing platform consists of two parts, including an appropriate PEC sensor and an electron/hole donor.[30] When the photoactive material is excited by light, the electron–hole pair will be generated, and the charge recombination will reduce the photoelectric conversion efficiency. However, in the presence of the electron donor, the pores are cleared, resulting in a significant enhancement of the photocurrent signal. Dopamine (DA), an amine neurotransmitter, has been used as an electron donor for photoelectric materials because it is oxidized to generate electrons when it is adsorbed on the receptor.[31] In this study, DA was selected as the electron donor and directly added in the system in advance.

In general, the characteristics of photoactive materials determine the performance of PEC biosensors to a large extent.

[a]School of Chemistry and Chemical Engineering, Institute of Environmental Science, Shanxi University, Taiyuan 030006, China. E-mail: zl104@sxu.edu.cn

[b]School of Chemistry and Chemical Engineering, Jinzhong University, Jinzhong, 030619, China

[c]Institute of Molecular Science, Key Laboratory of Chemical Biology and Molecular Engineering of the Education Ministry, Shanxi University, Taiyuan, Shanxi, 030006, China

[d]School of Chemistry and Chemical Engineering, Southeast University, Nanjing 211189, China

† Electronic supplementary information (ESI) available. See DOI: 10.1039/d1ra04275k

Among them, semiconductor nanomaterials have been regarded as the most promising photoactive materials because of their special valence band (VB) and conduction band (CB) electronic states as well as suitable band gaps.[32] Graphitic carbon nitride (g-C_3N_4), a metal-free semiconducting polymer possessing the strong covalent bonding within adjacent C–N layers, is a two-dimensional layered material similar to graphene.[33] In addition, the formation of the p-conjugated graphitic planes due to sp^2 hybridization is the key to making g-C_3N_4 possessing the smallest direct band gap width of 2.7 eV, which results in excellent chemical and thermal stability of g-C_3N_4 under 460 nm light irradiation.[34–36] PCN-222, with zirconium (Zr) as the metal center and porphyrin as the organic ligand, is an important branch of metal–organic frameworks (MOFs) material.[37–40] In comparison with porphyrin ligand, the HOMO–LUMO energy gap of PCN-222 is smaller, which is beneficial for a photoinduced electron transfer (PET) process.[41] Therefore, PCN-222 provides a platform to prepare new heterogeneous catalysis with highly accessible external and internal surface and evenly distributed active sites. However, we found that when g-C_3N_4 or PCN-222 was applied to the photoelectrochemical sensing platform alone, the photoelectronic performance would be relatively poor even in the presence of DA. But the synergy between g-C_3N_4 with PCN-222 resulted in the generation of obvious photocurrent signal.

In this work, a novel strategy was explored that integrating g-C_3N_4 to PCN-222 by simple method of physical microwave mixing. And then, we designed a label-free photocurrent strategy for the efficient and ultrasensitive detection of KAM. In addition, the method can be used to specifically identify the content of KAM in milk and KAM injection.

2 Experimental

2.1 Reagents

Zirconium(IV) chloride, *meso*-tetra (4-carboxyphenyl) porphyrin (TCPP) benzoic acid, *N*,*N*-dimethylformamide (DMF), ascorbic acid (AA), dopamine (DA), *N*-2-hydroxyethylpiperazine-*N*′-2-ethanesulfonic acid (HEPES), potassium chloride (KCl), urea (AR, 99%), sodium sulfate solution (Na_2SO_4, 0.1 M) were supplied by Aladdin (Shanghai, China). Amoxicillin (AMX), kanamycin sulfate (KAM), enrofloxacin (NFX), erythromycin (ERY), chloramphenicol (CRY) and tetracycline (TE) were all antibiotics from Aladdin (Shanghai, China). All reagents were of analytical reagent grade and used as received. Deionized water was from Millipore water purification system (≥18 MΩ cm^{-1}, Milli-Q, Millipore).

2.2 Apparatus

All the PEC measurements were carried on a RST5200F electrochemical workstation (Zhengzhou Shi Ruisi Instrument Technology Co., Ltd.). Xenon lamp (λ > 420 nm) was used as the irradiation source. The fluorine-doped SnO_2 conductive glass (FTO) (15 × 50 mm, resistance = 10 Ω) was purchased from Wuhan Crystal Solar Energy Technology Co. Ltd. The UV spectrum was measured on the TU-1950 spectrophotometer (Beijing, China). Electron spectrometer (Shimadzu, Japan) was used to obtain X-ray photoelectron spectroscopy (XPS) data. The Transmission electron microscopy (TEM) image was obtained from JSM-7900F (Japan). A Rigaku Dmax 2000 X-ray diffractometer containing graphite monochromatic CuKα radiation (λ = 0.154 nm) was used to obtain the X-ray diffraction pattern (XRD). Fourier transform infrared spectroscopy (FTIR) was recorded on a Bruker IR spectrometer.

2.3 Preparation of PCN-222@g-C_3N_4

The preparation method of g-C_3N_4 adopted the reported method.[42] The urea was heated in a muffle furnace at a rate of 5 °C min^{-1} to 500 °C for 3 h. The yellow product obtained (g-C_3N_4) was collected for future use. $ZrCl_4$ (75 mg), TCPP (30 mg) and benzoic acid (1750 mg) were dissolved in 10 mL DMF, and the above solution was ultrasound dissolved in a glass vial. The above mixture was heated to 120 °C, for 48 h. The synthesized PCN-222 was cooled to room temperature, purple needle crystals were collected under centrifugal conditions. 0.005 g g-C_3N_4 dissolved in 5 mL methanol, ultrasound dissolve for 20 h. 0.005 g PCN-222 dissolved in 5 mL methanol, ultrasound dissolve for 2 h. Mixing g-C_3N_4 solution and PCN-222 solution at a mass ratio of 1 : 0.75, ultrasound dissolve for 2 h to prepare composite solution, and reserve at 4 °C.

2.4 Preparation of modified electrode

The FTO electrode was respectively cleaned in acetone, ethanol and secondary water for 30 min sequentially. The cleaned FTO electrode was stored in ethanol solution. PCN-222@g-C_3N_4 was modified onto the FTO electrode by drop casting. PCN-222@g-C_3N_4/FTO electrode, Pt electrode and Ag/AgCl constituted a three-electrode system, and the 0.01 M HEPES solution used as electrolyte. Turned on/off the Xe lamp light source for 60 s, and tested for 60 seconds with the light source turned on. Repeated the above experiment several times until the photocurrent was stable. The aqueous solution of KAM was added by dropping to the electrolyte, and allowed to standing for 5 min for detection.

3 Results and discussion

3.1 Detection strategy

Under simulated sunlight, the PEC sensor for detection KAM was developed based on rod-shaped PCN-222 and flake-shaped g-C_3N_4 (Scheme 1). The composite of g-C_3N_4 and PCN-222 can

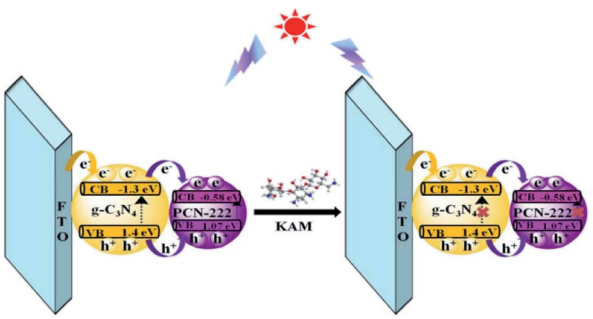

Scheme 1 The mechanism of charge recombination suppression-based photoelectrochemical strategy for the detection of KAM.

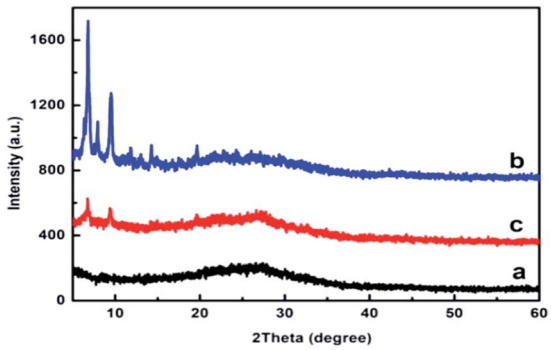

Fig. 1 XRD spectra of g-C_3N_4 (a), PCN-222 (b), PCN-222@g-C_3N_4 (c).

effectively reduce carrier recombination and improve the photocatalytic performance. The addition of KAM can effectively inhibit the electron transfer behavior to reduce the photocurrent in the system.

3.2 Phase and chemical structure

3.2.1 XRD analysis. The XRD patterns of synthesized compounds are displayed in Fig. 1. The strongest diffraction peak of g-C_3N_4 is about 27.4° (curve *a*), which is due to the interlayer stacking effect of g-C_3N_4.[43] The main diffraction peaks of PCN-222 are 2.4°, 4.8°, 7.1° and 9.8° (curve *b*), which match the previously reported simulated XRD patterns of PCN-222.[44] PCN-222@g-C_3N_4 contains all characteristic diffraction peaks of PCN-222 and g-C_3N_4, indicating that PCN-222 has been successfully compounded with g-C_3N_4, and their structure is reserved (curve *c*).

3.2.2 FTIR and XPS analysis. The infrared characterization is shown in Fig. 2A. In pure PCN-222 (curve *a*), the vibration peaks appearing at 1604.29 cm^{-1}, 1414.54 cm^{-1}, and 825.7 cm^{-1} have a small deviation from other literature, which may be caused by the residual of solvent molecules in the pure PCN-222 channel.[45] Pure g-C_3N_4 has three features at 3176.8 cm^{-1}, 1200–1700 cm^{-1}, and 811.2 cm^{-1} (curve *b*). The stretching vibration of the N–H bond is obvious at 3176.8 cm^{-1}. The peak at 1200–1700 cm^{-1} belongs to CN heterocycles in g-C_3N_4, the peak at 811.21 cm^{-1} is related to the triazine ring structure.[46] All the main characteristic peaks of g-C_3N_4 and PCN-222 appear in of the composite PCN-222@g-C_3N_4 (curve *c*).

XPS technology can be used to analyze the surface elements of the sample. The main elements contained in the PCN-222@g-C_3N_4 composite are C 1s, N 1s, O 1s and Zr 3d (Fig. S1†). C 1s contains two main peaks, the peak at 284.6 eV corresponds to the C–C bond of the indeterminate carbon or sp2 hybridization on the surface of the substance, and the peak at 288.3 eV corresponds to the N–C=N bond (Fig. 2B). N 1s contains two main peaks, the peak at 398.7 eV belongs to the C=N–C bond, the peak at 400.2 eV corresponds to the N–$(C)_3$ bond (Fig. 2C). The peaks of Zr 3d at 182.9 eV and 185.35 eV correspond to Zr $3d_{5/2}$ and Zr $3d_{3/2}$ (Fig. 2D).[47]

3.3 Morphological characterization

Transmission electron microscopy (TEM) and scanning electron microscopy (SEM) characterized the morphology of the materials. Pure g-C_3N_4 has tulle-like thickness, the TEM image shows that g-C_3N_4 has a large specific surface area and a smooth surface (Fig. 3A). The SEM morphology of pure g-C_3N_4 has many thin corrugated sheets that provide predominate anchor sites for loading of PCN-222 (Fig. 3D). Pure PCN-222 exists uniformly in a three-dimensional rod shape of 3–4 μm (Fig. 3B and E). After PCN-222 was combined with g-C_3N_4, PCN-222 was successfully reorganized on the surface of g-C_3N_4 (Fig. 3C and F), the recombined PCN-222@g-C_3N_4 prolonged the charge transfer rate, thereby enhancing the photoelectric activity.

3.4 Material properties

The solid UV of PCN-222 and g-C_3N_4 is shown in Fig. S2.† Pure g-C_3N_4 has strong absorption at 200–460 nm, and the band gap of g-C_3N_4 is about 2.7 eV (Fig. 4A). PCN-222 has relatively strong absorption in the range of 200–800 nm, it shows that PCN-222 can perform electronic transition under visible light. From Fig. 4B, the band gap of pure PCN-222 is obtained in 1.65 eV. The Mott–Schottky measurement is used to determine the energy band position of a substance, the positive slop of Mott–Schottky curves proved that PCN-222 and g-C_3N_4 are both n-type semiconductors. The corresponding conduction band position

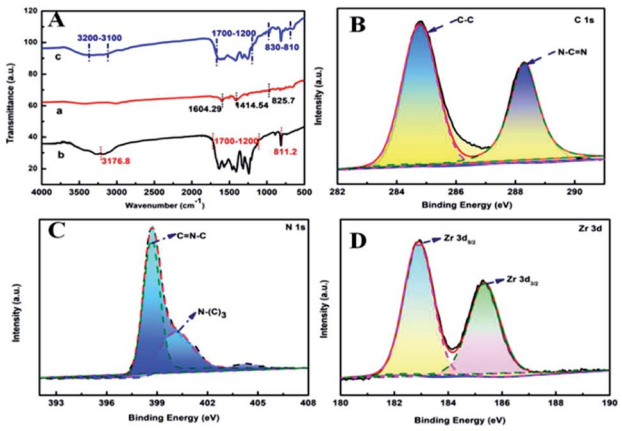

Fig. 2 (A) FTIR spectra of (a) PCN-222, (b) g-C_3N_4, and (c) PCN-222@g-C_3N_4 materials. Binding energy regions of (B) C 1s, (C) N 1s, (D) Zr 3d.

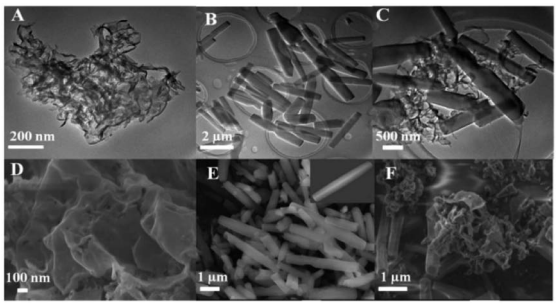

Fig. 3 TEM of (A) g-C_3N_4 (B) PCN-222 (C) PCN-222@g-C_3N_4; SEM of (D) g-C_3N_4 (E) PCN-222 (inset: single PCN-222 nanorod) (F) PCN-222@g-C_3N_4.

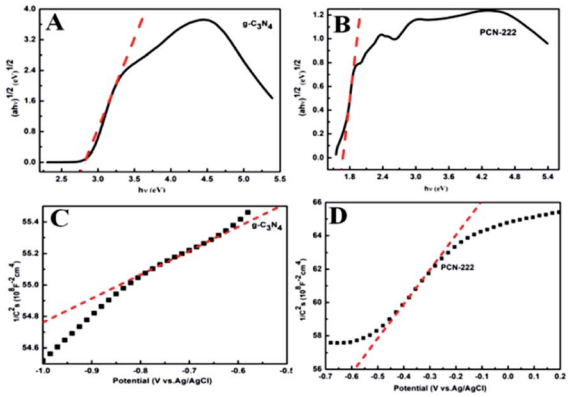

Fig. 4 UV-vis diffuse absorbance spectra of (A) g-C_3N_4 (B) PCN-222. Mott–Schottky plots of (C) g-C_3N_4 (D) PCN-222.

of the specimen lies at ~−1.3 eV and −0.58 eV (*versus* NHE) for pure g-C_3N_4 (Fig. 4C) and PCN-222 (Fig. 4D), respectively. Therefore, the valence and conduction bands of g-C_3N_4 are 1.4 eV and −1.3 eV. the valence and conduction bands of PCN-222 are 1.07 eV and −0.58 eV.

To study the performance of this sensor in the detection of KAM, the pH, modification amount, reducing agent and ratio were optimized. The result was shown in Fig. S3.† When the modification amount was 60 μL and pH = 6.4, the photocurrent showed the highest value. The photocurrent intensity successively was DA, H_2O_2, AA, L-Cys, indicating that DA was the most excellent substance as an electron donor. A rate of g-C_3N_4 to PCN-222 is 1 : 0.75 had strongest photocurrent, it showed that the mass ratio of 1 : 0.75 was the best condition. The possible reason is that PCN-222 can supply more holes to join in photoelectrochemical processes. However, a large number of PCN-222 prevents the transfer of photogenerated electrons on the surface.

3.5 Sensor performance

Electrochemical impedance spectroscopy (EIS) technique is used to characterize the properties of various materials modified (Fig. 5A). The blank electrode FTO was 65 Ω (curve *a*). When g-C_3N_4 was applied to the FTO electrode, the resistance value of g-C_3N_4/FTO was 55 Ω (curve *b*). When PCN-222 was applied onto the FTO electrode, the resistance value decreased significantly to 45 Ω (curve *c*). PCN-222@g-C_3N_4 was present on the FTO electrode, the resistance value dropped to 35 Ω (curve *d*). This

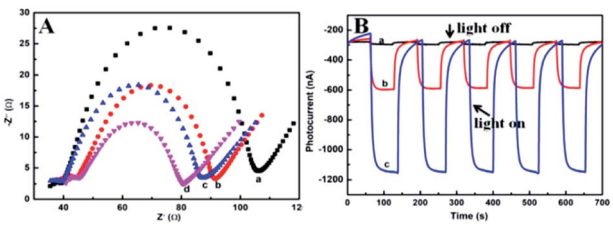

Fig. 5 (A) EIS of (a) FTO, (b) g-C_3N_4/FTO, (c) PCN-222/FTO, (d) PCN-222@g-C_3N_4/FTO; (B) photocurrent response curve (a) g-C_3N_4/FTO, (b) PCN-222/FTO, (c) PCN-222@g-C_3N_4/FTO.

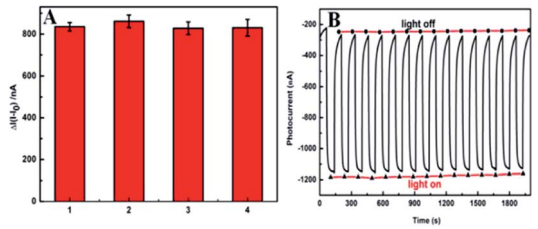

Fig. 6 (A) Reproducibility of the prepared sensor; (B) detecting the stability of KAM sensor.

was consistent with our experimental results. As shown in Fig. 5B, the composite PCN-222@g-C_3N_4 had higher photocurrent than pure PCN-222 and pure g-C_3N_4, indicating that the composite had a better light response.

Obviously, the sensor was also examined four individual photoelectrodes. The sensors containing 100 nM KAM displayed reproducible photocurrent responses (Fig. 6A). After 15 times testing based on the off–on irradiation cycle, the photocurrent intensity remained 94.7% of the initial one which shows accredited stability (Fig. 6B). All these above results verified that the as-prepared PCN-222@g-C_3N_4 composite had good reproducibility and stability.

Comparing the response of PCN-222, g-C_3N_4 and PCN-222@g-C_3N_4 to antibiotics, it was found that PCN-222@g-C_3N_4 had a good response to KAM (Fig. S4†). Under the optimal conditions, the analytical performance of the designed PEC sensor was tested. As shown in Fig. 7A, we can observe that the photocurrent decreased with the increase of KAM concentration. The corresponding linear graph is shown in Fig. 7B, and the corresponding calibration curve is shown in Fig. 7C ($\Delta I = I - I_0$, I: photocurrent when KAM is added I_0: photocurrent without KAM). The concentration of ΔI and KAM has a linear relationship between 1 to 1000 nM, the detection limit is 0.127 nM (3σ), the linear regression equation is ΔI (nA) = 113.33 log C_{KAM} + 89.45 (R^2 = 0.996). Compared with the existing methods, the PEC sensor for KAM detection has a lower detection limit and a wider linear range (Table S1†). Fig. 7D displays the effect of other antibiotics (such as

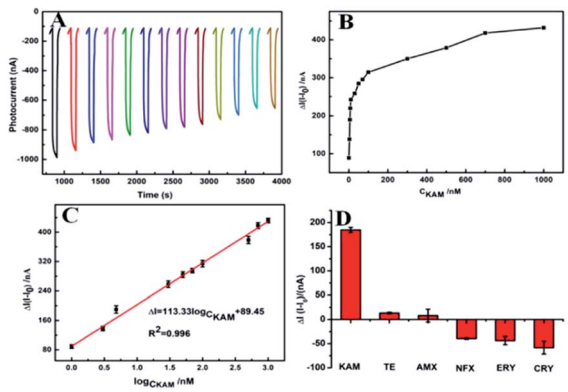

Fig. 7 (A) Photocurrent response at different contents of KAM, concentration from 1–1000 nM; (B) photocurrent linear curve; (C) linear calibration curve for photocurrent; (D) response of the prepared photoelectric sensor to different antibiotics.

Table 1 Test results of kanamycin sulfate in veterinary injection and milk

Sample	Added (nM)	Found (nM)	Recovery (%)	RSD (%)
Milk	5	5.4	92.60	2.10
	50	50.5	99.01	1.90
	100	102.6	97.47	1.87
Injection	5	5.25	95.24	1.70
	25	25.12	99.52	1.43
	250	249.74	100.10	1.46

AMX, NFX, ERY, CRY, and TE) on KAM detection. It can be seen that these antibiotics had little effect on the detection of KAM at the same concentration.

3.6 Detection of KAM in kanamycin sulfate injection (for veterinary use) and milk

In order to evaluate the applicability of the sensor prepared in the actual sample, the PCN-222@g-C_3N_4/FTO sensor was used to determine the KAM concentration in the injection. Diluted a certain amount of milk into 0.01 M HEPES solution, and added the KAM of different concentrations (5, 50, and 100 nM) for the spike recovery test. As shown in Table 1, the recovery rate reached 92.60–99.01%, the relative standard deviation (RSD, $n = 3$) was 1.87–2.10%. The kanamycin sulfate injection was diluted 10 times and added dropwise to the 0.01 M HEPES solution. After repeated determination three times, a satisfactory recovery rate of 95.24–100.10% was obtained, and the relative standard deviation (RSD, $n = 3$) was 1.43–1.70%.

4 Conclusions

In summary, we have designed a new double n-type of PEC for efficient and ultrasensitive detection of KAM. The PCN-222@g-C_3N_4 nanocomposite was used as photoelectric material to obtain stronger photoelectric signal, which was mainly attributed to assisted and cooperative effect between g-C_3N_4 and PCN-222. The so-obtained PCN-222@g-C_3N_4 was characterized separately by UV, TEM, XRD, XPS, and FTIR. It was discovered that the nanocomposite distributed on the electrode surface uniformly. Particularly, that photoelectrochemical tests showed that g-C_3N_4 could present dramatically enhanced photocurrent response of PCN-222. The PCN-222@g-C_3N_4 showed that the initial photocurrent is 2.78 times and 49 times compared with pure PCN-222 and g-C_3N_4, respectively. The designed sensor showed low detection limit, good repeatability and selectivity for the detection of KAM. The designed nanocomposite sensing platform can pave the way for PEC-based applications and overcome many problems in the material development process. The simplicity, stability and repeatability of this method provide a broad prospect for photoelectric sensing and monitoring platforms.

Conflicts of interest

There are no conflicts to declare.

Acknowledgements

The project was supported by the National Natural Science Foundation of China (21575083), Jinzhong College "1331 Project" Innovation Team (jzxycxtd2019007) the 12th "Hundred Talents Plan" in Shanxi Province (128,129), the 2019 Graduate Education Innovation Program (2019SY018). And we are very grateful to Prof. Feng for providing us with MOFs.

Notes and references

1 E. Adams, J. Dalle, E. D. Bie, I. D. Smedt and J. Hoogmartens, *J. Chromatogr. A*, 1997, **766**, 133.
2 Q. Luo, K. Qin, F. Liu, X. Zheng, Y. Ding, C. Zhang, M. Xu, X. Liu and Y. Wei, *Analyst*, 2021, **146**, 1965–1972.
3 H. Wang, W. Wu, D. Wei, Z. Guo and S. Wang, *J. Electroanal. Chem.*, 2014, **735**, 136–141.
4 H. Shuang, B. Li, Z. Song, S. Pan, Z. Zhang, Y. Hui, S. Zhu and G. Xu, *Analyst*, 2017, **142**, 218.
5 B. J. Stoll, *J. Pediatr.*, 2012, **160**, 344.
6 L. Ma, N. Sun, C. Tu, Q. Zhang and A. Diao, *RSC Adv.*, 2017, **7**, 38512–38518.
7 Y. Yao, C. M. Jiang and J. F. Ping, *Biosens. Bioelectron.*, 2019, **123**, 178–184.
8 J. Yu, W. X. Tang, F. Wang, F. Zhang, Q. J. Wang and P. G. He, *Sens. Actuators, B*, 2020, **311**, 127857.
9 B. Blanchaert, E. Poderós Jorge, P. Jankovics, E. Adams and A. Van Schepdael, *Chromatographia*, 2013, **76**, 1505–1512.
10 I. Nina and S. Stefan, *J. AOAC Int.*, 1999, 1017.
11 C. K. Wang, D. Chen, Q. Q. Wang and R. Tan, *Biosens. Bioelectron.*, 2017, **91**, 262–267.
12 H. Li, D. E. Sun, Y. J. Liu and Z. H. Liu, *Biosens. Bioelectron.*, 2014, **55**, 149–156.
13 M. A. Rostagno, M. D'Arrigo and J. A. Mart'nez, *TrAC, Trends Anal. Chem.*, 2010, **29**, 553–561.
14 F. Bottari, R. Blust and K. D. Wael, *Curr. Opin. Electrochem.*, 2018, **10**, 136–142.
15 W. J. Guo, N. Sun, X. L. Qin, M. S. Pei and L. Y. Wang, *Biosens. Bioelectron.*, 2015, **74**, 691–697.
16 Y. L. Zhou, F. Li, H. W. Wu, Y. Chen, H. S. Yin, S. Y. Ai and J. Wang, *Sens. Actuators, B*, 2019, **296**, 126664.
17 J. Yu, W. X. Tang, F. Wang, F. Zhang, Q. J. Wang and P. G. He, *Sens. Actuators, B*, 2020, **311**, 127857.
18 Y. Yao, T. Y. Chen, W. Mao, Y. Zhong, S. S. Dai, X. M. Zeng, C. Liu, S. Tang, F. Qiao, E. Shi, W. Shen and H. K. Lee, *Sens. Actuators, B*, 2021, **343**, 130082.
19 X. L. Qin, Y. Yin, H. J. Yu, W. J. Guo and M. S. Pei, *Biosens. Bioelectron.*, 2016, **77**, 752–758.
20 A. Sharma, G. Istamboulie, A. Hayat, G. Catanante, S. Bhand and J. L. Marty, *Sens. Actuators, B*, 2017, **245**, 507–515.
21 F. Hong, X. X. Chen, Y. T. Cao, Y. R. Dong, D. Z. Wu, F. T. Hu and N. Gan, *Biosens. Bioelectron.*, 2018, **112**, 202–208.
22 I. Willner, F. Patolsky and J. Wasserman, *Angew. Chem., Int. Ed.*, 2001, **40**(10), 1861–1864.
23 V. Pardo-Yissar, E. Katz, J. Wasserman and I. Willner, *J. Am. Chem. Soc.*, 2003, **125**, 622–623.

24 F. A. L. Laskowski, M. R. Nellist, J. Qiu and S. W. Boettcher, *J. Am. Chem. Soc.*, 2019, **141**, 1394–1405.
25 L. n. Zhao, Z. Li, H. You and W. r. Li, *Int. J. Hydrogen Energy*, 2021, **46**, 18305–18317.
26 N. Haddour, J. Chauvin, C. Gondran and S. Cosnier, *J. Am. Chem. Soc.*, 2006, **128**, 9693–9698.
27 S. Wu, H. Song, J. Song, C. He, J. Ni, Y. Zhao and X. Wang, *Anal. Chem.*, 2014, **86**, 5922–5928.
28 H. Li, J. Li, Q. Xu and X. Hu, *Anal. Chem.*, 2011, **83**, 9681–9686.
29 L. Fan, C. Zhang, H. Shi and G. Zhao, *Biosens. Bioelectron.*, 2019, **124–125**, 8–14.
30 W. W. Zhao, Z. Y. Ma, D. Y. Yan, J. J. Xu and H. Y. Chen, *Anal. Chem.*, 2012, **84**, 10518–10521.
31 T. M. Prado, A. Carrico, F. H. Cincotto, O. Fatibello-Filho and F. C. Moraes, *Sens. Actuators, B*, 2019, **285**, 248–253.
32 P. P. Li, Y. Cao, C. J. Mao, B. K. Jin and J. J. Zhu, *Anal. Chem.*, 2019, **91**, 1563–1570.
33 M. Zhang, Y. Liu, D. Zhang, T. Chen and Z. Li, *Anal. Chem.*, 2017, **89**, 8064–8069.
34 X. Li, L. Zhu, Y. Zhou, H. Yin and S. Ai, *Anal. Chem.*, 2017, **89**, 2369–2376.
35 X. Zhang, X. Xie, H. Wang, J. Zhang, B. Pan and Y. Xie, *J. Am. Chem. Soc.*, 2013, **135**, 18–21.
36 G. Gao, Y. Jiao, E. R. Waclawik and A. Du, *J. Am. Chem. Soc.*, 2016, **138**, 6292–6297.
37 P. Deria, D. A. Gomez-Gualdron, I. Hod, R. Q. Snurr, J. T. Hupp and O. K. Farha, *J. Am. Chem. Soc.*, 2016, **138**, 14449–14457.
38 R. Hariri and S. Dehghanpour, *J. Phys. Chem. Solids*, 2021, **155**, 110126.
39 S. Nazri, M. Khajeh, A. R. Oveisi, R. Luque, E. Rodríguez-Castellón and M. Ghaffari-Moghaddam, *Sep. Purif. Technol.*, 2021, **259**, 118197.
40 J. He, X. Wu, Z. Long and X. Hou, *Microchem. J.*, 2019, **145**, 68–73.
41 H. J. Jia, D. X. Ma, S. W. Zhong, L. J. Li, L. Li, L. Xu and B. Y. Li, *Chem. Eng. J.*, 2019, **368**, 165–174.
42 Z. P. Li, W. X. Dong, X. Y. Du, G. M. Wen and X. J. Fan, *Microchem. J.*, 2020, **152**, 104259.
43 P. Yang, J. C. Wang, G. Z. Yue, R. Z. Yang, P. X. Zhao, L. J. Yang, X. C. Zhao and D. Astrucc, *J. Photochem. Photobiol., A*, 2020, **388**, 112169.
44 D. W. Feng, Z. Y. Gu, J. R. Li, H. L. Jiang, Z. W. Wei and H. C. Zhou, *Angew. Chem., Int. Ed.*, 2012, **51**, 10307–10310.
45 W. L. Tan, T. Wei, J. Huo, M. Loubidi, T. T. Liu, Y. Liang and L. B. Deng, *ACS Appl. Mater. Interfaces*, 2019, **11**, 36782–36788.
46 L. T. Ma, H. Q. Fan, K. Fu, S. H. Lei, Q. Z. Hu, H. T. Huang and G. P. He, *ACS Sustainable Chem. Eng.*, 2017, **5**, 7093–7103.
47 S. Biswas, Y. L. Chen, Y. Xie, X. Sun and Y. Wang, *Anal. Chem.*, 2020, **92**, 4566–4572.